Monthly resolved modelled oceanic emissions of carbonyl sulfide and carbon disulfide for the period 2000-2019

Sinikka T. Lennartz[1], Michael Gauss[2], Marc von Hobe[3], Christa A. Marandino[4]

[1]Institute for Chemistry and Biology of the Marine Environment, University of Oldenburg, Carl-von-Ossietzky-Straße 9-11,
26129 Oldenburg, Germany
[2]Norwegian Meteorological Institute, PO 43 Blindern, 0313 Oslo, Norway
[3]Institute for Energy and Climate Research (IEK-7), Forschungszentrum Jülich GmbH, 52425 Jülich, Germany
[4]Geomar Helmholtz-Centre for Ocean Research Kiel, Düsternbrooker Weg 20, 24105 Kiel, Germany

Correspondence to: Sinikka T. Lennartz (sinikka.lennartz@uni-oldenburg.de)

Abstract. Carbonyl sulfide (OCS) is the most abundant, long-lived sulphur gas in the atmosphere and a major supplier of sulfur to the stratospheric sulfate aerosol layer. The short-lived gas carbon disulfide (CS_2) is oxidized to OCS and constitutes a major indirect source to the atmospheric OCS budget. The atmospheric budget of OCS is not well constrained due to a large missing source needed to compensate for substantial evidence that was provided for significantly higher sinks. Oceanic emissions are associated with major uncertainties. Here we provide a first, monthly resolved ocean emission inventory of both gases for the period 2000-2019 (available at https://doi.org/10.5281/zenodo.4297010)(Lennartz et al., 2020a). Emissions are calculated with a numerical box model (resolution 2.8° x 2.8° at equator, T42 grid) for the surface mixed layer. We find that interannual variability in OCS emissions is smaller than seasonal variability, and is mainly driven by variations in chromophoric dissolved organic matter (CDOM), which influences both photochemical and light-independent production. A comparison with a global database of more than 2500 measurements reveals overall good agreement. Emissions of CS_2 constitute a larger sulfur source to the atmosphere than OCS, and equally show interannual variability connected to variability of CDOM. The emission estimate of CS_2 is associated with higher uncertainties, as process understanding of the marine cycling of CS_2 is incomplete. We encourage the use of the data provided here as input for atmospheric modelling studies to further assess the atmospheric OCS budget and the role of OCS in climate.

1 Introduction

The trace gases carbonyl sulfide (OCS) and carbon disulfide (CS_2) are naturally produced in the ocean and emitted to the atmosphere (Ferek and Andreae, 1983; Kettle et al., 2001; Khalil and Rasmussen, 1984; Watts, 2000). CS_2 is oxidized to a large extend to OCS (~82% on a molecular basis) within hours to days after emission and thus constitutes a large indirect source in the atmospheric OCS budget (Chin and Davis, 1993; Stickel et al., 1993). OCS is the most abundant sulfur gas in the atmosphere with an average mixing ratio of ca. 480 ppt at land-based time series stations (Montzka et al., 2007) and ca. 550 ppt in the marine boundary layer (Lennartz et al., 2020b). The sources and sinks of atmospheric OCS are important in two

contexts: first, OCS is transported to the stratosphere due to its long tropospheric lifetime of 1.5 to 3 years (Montzka et al., 2007), where it is a major precursor of sulfate aerosols (Brühl et al., 2012; Kremser et al., 2016; Turco et al., 1980). The stratospheric sulfate aerosol layer influences the radiative budget by increasing the planetary albedo, and in addition provides surfaces for ozone catalysing reactions (Solomon et al., 2011, 2015). Second, OCS has been suggested as a promising proxy

35 to constrain the terrestrial CO_2 uptake on a global scale using inverse atmospheric modelling (Berry et al., 2013; Stimler et al., 2010; Whelan et al., 2018). In order to understand the dynamics of the sulfate aerosol layer and to apply OCS as a proxy for gross primary production, the quantification of OCS sources and sinks to the atmosphere on a global scale is required.

Currently, oceanic emissions are associated with the highest uncertainties among sources in the atmospheric OCS budget (Kremser et al., 2016; Whelan et al., 2018). Evidence for increasing the vegetation sink led to a missing source the budget

40 (Suntharalingam et al., 2008), and oceanic emissions have been suggested to account for a gap of 600-800 Gg S yr^{-1} (Berry et al., 2013; Glatthor et al., 2015; Kuai et al., 2015). Global oceanic emission estimates extrapolated from measurements range from -16 Gg S yr^{-1} (Weiss et al., 1995b) to 320 Gg S yr^{-1} (Rasmussen et al., 1982). Surface ocean models that are largely in agreement with observations report direct OCS emissions from the oceans of 41 Gg S yr^{-1} (Kettle et al., 2002) to 130 Gg S yr^{-1} (Lennartz et al., 2017). Generally, surface seawater concentrations of OCS are too low to sustain emissions that would close

45 the budget (Lennartz et al., 2017, 2020b). A detailed description of the marine emissions of OCS and its precursor CS_2 can serve as an input to modelling studies, and thus help to identify the missing source. However, current marine emission inventories rely on modelled climatological averages, and do not resolve interannual variability (Kettle et al., 2002; Lennartz et al., 2017).

Models resolving the marine cycling of both trace gases are powerful tools to assess interannual variability of marine emissions

50 through variations in the factors influencing production and consumption of the gas in seawater. The processes determining OCS concentration in the surface ocean are comparably well understood, and include a photochemical production process, a light-independent dark production term, degradation by hydrolysis and air-sea exchange. Diapycnal fluxes into and out of the mixed layer seem to be of minor importance, at least in tropical waters (Lennartz et al., 2019). The photochemical OCS production involves UV-radiation interactions with chromophoric dissolved organic matter (CDOM) (Ferek and Andreae,

55 1984; Modiri Gharehveran and Shah, 2018; Pos et al., 1998). Apparent quantum yields (AQY) decrease with increasing wavelength, but show orders of magnitude differences between locations (Cutter and Radford-Knoery, 1993; Weiss et al., 1995a; Zepp and Andreae, 1994). Reaction mechanisms involving thiyl radicals have been identified from precursor molecules such as cysteine, cystine and methionine (Modiri Gharehveran and Shah, 2018; Pos et al., 1998). However, the complexity of the natural mixture of dissolved organic sulfur molecules in the ocean (Ksionzek et al., 2016) makes the determination of a

60 photoproduction rate constant on a global scale difficult. Following an approach initially suggested by von Hobe et al., (2003), the photoproduction rate constant was scaled according to the CDOM absorption coefficient at 350 nm (a_{350}) in the global surface ocean box model used in this study (Lennartz et al., 2017). This approach led to good agreement of climatological mean modelled concentration with measured sea surface OCS concentrations. The mechanism for OCS dark production is not well known, and two not mutually exclusive hypotheses have been suggested, i.e. dark production being connected to abiotic

65   radical reactions (von Hobe et al., 2001) or microbial remineralisation processes (Cutter et al., 2004). The dependency of the

dark production rate on CDOM absorption and temperature shows good agreement across various biogeochemical regimes

(Lennartz et al., 2019). Hydrolysis is the main chemical sink for OCS in the mixed layer. In both an acid and an alkaline

reaction, OCS hydrolysis yields CO_2 and sulfide (Elliott et al., 1987). This reaction is strongly temperature dependent, leading

to e-folding lifetimes between several hours in warm waters and several days in cold, high latitude waters (Elliott et al., 1989).

70   The temperature dependency of this reaction has been reasonably well described by independent laboratory and field studies

(Cutter and Radford-Knoery, 1993; Elliott et al., 1989; Kamyshny et al., 2003).

CS_2 is present in seawater in picomolar concentrations, and measurements are generally sparse (Lennartz et al., 2020b). A

correlation between temperature and CS_2 concentration in surface waters is evident across several datasets (Lennartz et al.,

2019; Xie and Moore, 1999). CS_2 is produced by photochemical reactions as well, following a similar shape of the AQY-

75   wavelength spectrum as OCS (Xie et al., 1998). Precursor molecules such as cysteine, cystine, methionine and DMS have been

identified, and photochemical CS_2 production itself seems to be temperature dependent (Modiri Gharehveran and Shah, 2018).

Furthermore, there is evidence for a biological production of CS_2 by phytoplankton species, with varying yield from different

species (Xie et al., 1999), but the exact mechanism is unknown. Outgassing to the atmosphere is considered the most important

sink process for CS_2 in the mixed layer. The only chemical sink mechanism known so far is hydrolysis with a lifetime of

80   several years (Elliott, 1990). However, a chemical sink process in addition to air-sea gas exchange was needed to explain

observations along an Atlantic transect, with an e-folding lifetime of ca. 10 days (Kettle et al., 2001).

Here, we use existing models that include parameterizations of processes known to be relevant for each gas, and apply them

on a global scale, accounting for interannual variability in the forcing parameters. We present the first monthly resolved

inventory for marine OCS and CS_2 emissions for the period 2000-2019. We encourage the community to use these emissions

85   for atmospheric modelling studies in order to elucidate the atmospheric budget of OCS, assess variability in the supply to the

sulfate   aerosol   layer   and   determine   gross   primary   production   on   a   global   scale   (available   at:

https://doi.org/10.5281/zenodo.4297010)(Lennartz et al., 2020a).

2 Model description

A model version as described in Lennartz et al. (2017) is used to model the interannual variability in oceanic emissions for

90   OCS. A new model is developed to simulate oceanic emissions of CS_2. In both models, the surface ocean is divided into grid

boxes of 2.8 x 2.8° at the equator (T42 grid, Gaussian grid with ~310 km resolution at equator (NCAR, 2017)) that comprise

various depth layers of 1m thickness depending on the depth of the mixed layer in each grid box. Note that the model does not

resolve exchange of gases horizontally between the boxes (see Lennartz et al., 2017, for details).

The numerical model simulating OCS seawater concentration and emission includes the processes photochemical production

95    $\frac{d[OCS]_{photo}}{dt}$, dark production $\frac{d[OCS]_{dark}}{dt}$, hydrolysis $\frac{d[OCS]_{hydrolysis}}{dt}$ and air-sea exchange $\frac{d[OCS]_{ase}}{dt}$ according to equation (1) (Fig.

1):

$$\frac{d[OCS]}{dt} = + \frac{d[OCS]_{photo}}{dt} + \frac{d[OCS]_{dark}}{dt} - \frac{d[OCS]_{hydrolysis}}{dt} + \frac{d[OCS]_{ase}}{dt} \qquad (1)$$

100   Photochemical production is calculated as the product of UV radiation UV [W m^{-2}], the absorption coefficient of CDOM at 350 nm a_{350} [m^{-1}], and the photoproduction rate constant p integrated over the mixed layer depth (MLD) according to equation (2):

$$\frac{d[OCS]_{photo}}{dt} = \int_{-MLD}^{0} UV \cdot a_{350} \cdot p(a_{350}) dz \qquad (2)$$

105

The photochemical rate constant p is scaled with a_{350}, following a rational suggested by von Hobe et al., (2003), which reflects that a_{350} can be regarded as a proxy for both photosensitizer and sulfur source across large spatial scales. The linear dependence between a_{350} and p is calculated based on fits to observational data from three major ocean basins as described in Lennartz et al., (2017). This wavelength-integrated approach has been shown to reproduce both local measurements from several cruises

110   as well as global OCS observations (von Hobe et al., 2003; Lennartz et al., 2017). UV radiation below the sea surface is calculated according to solar radiation, zenith angle and wind speed following von Hobe et al. (2003) as described in Lennartz et al. (2017). The light field in each 1 m depth layer is calculated by reducing the incoming short-wave radiation depending on the local absorption coefficient a_{350}. Photochemical production is then computed for each layer individually, followed by integration over the entire mixed layer. This integration inherently assumes a well-mixed surface layer.

115   Dark production is calculated according to Lennartz et al. (2019). This reaction rate is an update of the original formulation by von Hobe et al. (2001), resulting in a semi-empirical relationship based on observations from a wider spatial range of observation than the initial study. In this formulation, the dark production rate depends on temperature and a_{350} (eq. 3):

$$\frac{d[OCS]_{dark}}{dt} = a_{350} \cdot 10^{-6} \cdot e^{\left(57.2 - \frac{16\,200}{SST}\right)} \qquad (3)$$

OCS hydrolysis is determined according to Elliott et al. (1989) and depends on temperature (SST), salinity (SSS) and the

120   proton activity $a[H^+]$, equivalent to 10^{-pH}, according to eq. (4) and eq. (5):

$$\frac{d[OCS]_{hydrolysis}}{dt} = [OCS] \cdot \left[\exp\left(24.3 - \frac{10\,459}{SST}\right) + exp\left(22.8 - \frac{6\,040}{SST}\right) \cdot \frac{K}{a[H^+]}\right] \qquad (4)$$

$$-log_{10}K = \frac{3046.7}{SST} + 3.7685 + 0.0035486 \cdot \sqrt{SSS} \qquad (5)$$

Air-sea exchange is calculated as the product of the concentration gradient between water and equilibrium concentration Δc and the transfer velocity k parametrized according to Nightingale et al. (2000):

125    $$\frac{d[OCS]_{ase}}{dt} = k \cdot \Delta c \qquad (6)$$

The equilibrium concentration is calculated according to de Bruyn et al. (De Bruyn et al., 1995). The transfer velocity is corrected for OCS with the Schmidt number, calculated based on the molar volume according to Hayduk and Laudie (1974).

The model is run with a time step of 2 hours. Results are evaluated after spin-up of one year.

The model for CS_2 includes the processes of photochemical production and a first order chemical sink, according to eq. (7).

130

$$\frac{d[CS_2]}{dt} = +\frac{d[CS_2]_{photo}}{dt} - \frac{d[CS_2]_{chem.sink}}{dt} + \frac{d[CS_2]_{ase}}{dt} \tag{7}$$

Photochemical production is calculated in the same way as for OCS, with an additional reduction factor r applied (eq. 8).

$$\frac{d[CS_2]_{photo}}{dt} = r \cdot \int_{-MLD}^{0} UV \cdot a_{350} \cdot p(a_{350}) dz \tag{8}$$

Xie et al. (1998) approximated that CS_2 photoproduction rates are about a factor of five smaller than OCS photoproduction
135 rates by comparing an experimentally derived AQY from CS_2 and OCS (r=0.2 in eq. 8). The two AQY were not measured at the same location, but in comparable water properties. Another study with simultaneous measurements of both gases reported varying factors between 0.2 and 0.014 (5 to 70 times smaller than OCS photoproduction) (Lennartz et al., 2019). Here, we scaled the reduction factor to obtain the best fit in the average concentration, resulting in a factor r=0.1 in eq. 8. Thus, the model reflects the similar shape of the AQY for both gases by assuming a constant ratio, but the scaling of the overall
140 magnitude of the photoproduction rate constant is chosen to obtain the best fit to observations from the database in Lennartz et al. (2020). A chemical sink according to the model formulation in Kettle (2000), i.e. with an e-folding lifetime of 10 days $\left(\frac{1}{k_{cs}}\right)$, was implemented according to eq. (9):

$$\frac{d[CS_2]_{chem.sink}}{dt} = k_{cs} \cdot (CS_2) \tag{9}$$

Air-sea exchange was calculated as described for OCS, using the CS_2 solubility according to De Bruyn et al. (1995).

145 As CS_2 cycling in the water column is not yet well understood, this model should be understood as a base model to be extended as soon as additional process rates and their dependencies become available.

3 Simulation set-up

Simulations are performed for the period 2000-2019. There are several changes in the forcing data compared to the climatological run in Lennartz et al. (2017). Here we use monthly resolved data for the period 2000-2019 for a_{350}, surface
150 shortwave radiation, surface temperature, wind speed and sea level pressure (Table 1). The meteorological data were obtained from the ERA5 reanalysis (more specifically, its product line 'ERA5 hourly data on single levels from 1979 to present', Hersbach et al., 2018) through the Copernicus Climate Change Service (https://climate.copernicus.eu/). One file per year and parameter, containing hourly data on 0.25° x 0.25° resolution, was downloaded. For wind speed, the zonal and meridional components of wind speed at 10m altitude (u_{10} and v_{10}, respectively) were downloaded separately and converted into wind
155 speed *ws* according to

$$ws = \sqrt{u_{10}{}^2 + v_{10}{}^2}$$

The post-processing of the meteorological data was done using CDO tools (climate data operators, version 1.9.8) (Schulzweida, 2019) and comprised the following steps:

160 a) the yearly files for each parameter were split into monthly files using the CDO flag 'splityearmon', resulting in 240 monthly files covering the 20-year period 2000 to 2019 for each parameter;

b) for each of the 240 months within the period, monthly-mean diel cycles of each meteorological parameter x were calculated using the CDO flag 'dhouravg', which calculates multi-day averages for every hour of a day as

$$\bar{x}_m(h) = \frac{1}{N_m} \sum_{d=1}^{N_m} x(d,h)$$

165 where m is the month (1 to 12), h is the hour of the day (1 to 24), d is the day of the month (1 to 28, 29, 30, or 31), and N_m is the number of days within month m;

c) the resulting fields were regridded from the regular 0.25° x 0.25° longitude-latitude grid into the spectral T42 grid (~2.8° x 2.8°) using the cdo flag 'remapcon2', which is a second-order conservative remapping method that takes into account all source grid points, both in longitude and latitude directions. Among the remapping methods available in CDO, 'remapcon2' was

170 considered the most appropriate to interpolate the selected meteorological parameters from a fine grid to a much coarser grid. Monthly forcing fields for CDOM are derived from Aqua MODIS satellite level 3 product 'absoprtion due to gelbstof and detritus at 443 nm' (NASA Goddard Space Flight Center, 2019), and converted to 350 nm with an exponential slope of 0.02 for the wavelength spectrum. Climatological values are used for salinity and mixed layer depth in a monthly resolution, which is the same for each month of the year throughout the simulation period, unchanged to Lennartz et al. (2017). The average diel

175 cycle of meteorological data is set to the 15th of each month (one value for every 2 hours). In between, data is interpolated separately for each time of the day, resulting in a continuous change of the amplitude of the diel cycles. The initial concentration for both gases is a constant value of 8 pmol L[-1] in all grid boxes. The model is spun up for one year, repeating the conditions of year 2000 prior to the simulation period.

4 Results

180 ### 4.1 Spatial and seasonal variability

Both gases show distinct spatial patterns in their annual concentration and emission averages, which reflect their marine cycling. For OCS, highest concentrations are present in cold, high latitude waters and shelf areas, whereas lowest concentrations prevail in warm, subtropical gyres where CDOM abundance in the water is low (Fig 2a). A latitudinal gradient with higher concentrations in high latitudes and low concentrations in tropical and subtropical waters reflects the temperature-

185 dependent degradation by hydrolysis. The degradation is strongest in warm waters, where the lifetime of OCS is on the order of hours, keeping concentrations low. This general pattern is in broad agreement with observations of the largest available database on seaborne OCS measurements (Lennartz et al., 2020). Annual mean emissions largely follow the spatial pattern of

OCS concentrations, with sources, i.e. flux from the ocean to the atmosphere, in shelf areas and high latitudes, and sink regions in the subtropical gyres (Fig. 2b). This general source and sink pattern does not change in all years covered in this period, but
190 the absolute concentrations and, hence, the magnitude of the emissions, show variability (see Section 4.2). The concentration pattern follows the seasonal pattern of radiation that drives photochemical production, resulting in an annual cycle with highest concentrations and emissions in temperate northern latitudes in boreal summer and highest concentrations and emissions in the Southern Ocean in austral summer. The globally integrated monthly emissions are highest in austral summer and lowest in austral winter, due to the high emissions in the Southern Ocean, which overcompensates the northern hemispheric summer
195 emissions by its large surface area, high wind speeds and high OCS seawater concentrations. The mean annual cycle follows the pattern of incoming surface radiation with highest concentration and emissions in the northern hemisphere in boreal summer and highest concentration and emissions in the Southern Ocean in austral summer. The amplitude of the mean seasonal cycle of OCS emissions is 21 Gg S yr^{-1} (Fig 3b). In July and August, the globally integrated net emissions are close to zero, similar to a previous budget using a similar model (Kettle et al., 2002).

200

CS_2 concentration show a different global pattern than OCS concentrations. CS_2 concentrations and emissions have hot spots in coastal and shelf regions, as well as in tropical and subtropical oceans, reflecting photoproduction as the main production process in the model. The tropical and subtropical areas show comparably low CS_2 concentrations (Fig. 4c), and their importance for globally averaged emissions mainly comes from the large oceanic surface area (Fig. 4d). Notably, CS_2
205 emissions in the western Pacific, where inverse modelling studies have located the missing source, are relatively low (Glatthor et al., 2015; Kuai et al., 2015). The hot spots being located in the tropical and subtropical regions with similar intensities of incoming radiation all year, leads to less seasonal variation in globally integrated emissions, i.e. an amplitude of 3.2 Gg S yr^{-1}. The ocean is a source of CS_2 to the atmosphere over the entire year, since emissions are calculated with an atmospheric mixing ratio of 0 ppt. Highest emissions occur in boreal winter, and the lowest in boreal summer.

210

4.2 Interannual variability

Surface concentrations of OCS show a similar spatial pattern across the period of 2000 to 2019, with interannual variability in the absolute concentration and, hence, emissions. Globally integrated emissions range from 77.3 Gg S yr^{-1} in 2001 to 142.1 Gg S yr^{-1} in 2017, with a mean of 110.3±20.3 Gg S yr^{-1} (Tab. 2). A significant increasing trend (p=0.028) is present in oceanic
215 emissions from the period 2003-2019 of about 1.7 g S yr^{-1} increase per year (Tab. 2). Note that for the trend analysis, we considered only the period 2003-2019, as CDOM seems to be one of the most important drivers of interannual variability (see below), and CDOM data are only available from 2003 onwards. Generally, the seasonal variability of OCS emissions is larger (range of mean annual cycle of 21 Gg S yr^{-1}) than the interannual variability (mean monthly variability of 8.4 Gg S month^{-1}) (Fig. 3). Interannual variability of the emissions in each month is largest during boreal spring (April, May, June) and fall
220 (October) (Fig. 3a). These months show the largest difference between minima and maxima during the whole period (grey

area in Fig 3a). The spatial pattern of interannual variability of OCS emissions shows highest variability, i.e. highest standard deviation among annual averages in each gridbox, at locations with high OCS concentrations and emissions (Fig. 2). These regions comprise the northern temperate and polar regions, the Southern Ocean, and shelf areas, especially those close to coastal upwelling regions and river plumes (Fig. 2). The standard deviation for OCS concentrations between annual averages

225   ranges from 0.22 at the oligotrophic gyres to 143.8 pmol L^{-1} at the highly dynamic coast off Alaska, USA (average standard deviation 3.4 pmol L^{-1}). The interannual variability also shows latitudinal differences. Polar regions in both Arctic and Antarctic waters display the largest seasonal cycles in OCS concentration, i.e. the highest annual variability (Fig 4), and at the same time also display highest interannual variability. Differences in mean concentrations (area weighted) in summer range between 72.8 pmol L^{-1} in June 2011 to 91.6 pmol L^{-1} in July 2017, i.e. ca. 20 pmol L^{-1} in the Arctic ocean (Fig. 4). Interannual

230   differences in mean monthly OCS concentrations become smaller with decreasing latitudes, and are lowest in tropical oceans where they range between 7.0 pmol L^{-1} in April 2002 and 8.5 pmol L^{-1} in April 2018 (south tropical) and 8.6 pmol L^{-1} in June 2015 and 9.0 pmol L^{-1} in June 2018 (north tropical). Due to their large surface area and medium surface OCS concentrations, southern temperate regions (23°S-66°S) have the largest integrated OCS emissions, followed by northern temperate regions (33°N-66°N) (Fig. 4). In temperate regions, largest interannual variability occurs during the months of maximum positive

235   emissions, with a range from 17.4 to 26.1 Gg S $month^{-1}$ in southern temperate regions in December, and 14.0 and 20.9 Gg S $month^{-1}$ in northern temperate regions in May. In summary, OCS concentrations and emissions show the highest interannual variability at time and locations where concentrations are high, and in systems that are inherently highly dynamic such as shelf regions.

240   Carbon disulfide concentrations are highest in shelf areas in the tropics and subtropics, and generally decrease towards high latitudes (Fig. 2c). The spatial pattern of the annually integrated emissions mirrors this picture (Fig. 2d). While the spatial pattern of concentrations and emissions is similar in each year, the absolute concentration and magnitude of emissions does show interannual variability (Fig. 3b). Emissions are calculated here with a boundary layer mixing ratio of zero (maximum possible emission) as is commonly done for other short-lived gases such as DMS (Lana et al., 2011), so the ocean is a CS_2

245   source at every location throughout the year. A little less than half of the sulfur in CS_2 is converted to OCS. Globally integrated emissions range from 160.0 Gg S yr^{-1} in 2002 to 189.7 Gg S yr^{-1} in 2017 (Tab. 2). Similar to OCS, an increasing trend of global CS_2 emissions for the period 2003-2019 is significant (p=0.0067). Emissions increase with 0.95 Gg S per year on average over the period 2003-2019. For globally integrated emissions, annual variability (mean range of 3.2 Gg S $month^{-1}$) is comparable to the interannual variability (3.2 Gg S yr^{-1}). This is different to OCS, where annual variability was higher than interannual

250   variability for globally integrated emissions. This difference is caused by the location of the respective hotspots of the produced gases: As OCS has its concentration and emission hot spots mainly in high latitudes, which experience a very seasonal light regime, its annual variability is high. The low concentrations of OCS (and corresponding low emissions) in the tropics result from the fast degradation by hydrolysis. In contrast, CS_2 has its concentration and emission hotspots mainly in low latitudes with more constant forcing, and hence displays smaller annual variability. The interannual variability of CS_2 emissions among

255   single months has a similar magnitude throughout the year (grey shaded area in Fig. 3d). Maximum monthly mean concentrations of CS_2 vary the most in the summer months of the northern temperate regions (23°-66°N) from 4.3 Gg S month^{-1} in June 2011 and 6.0 Gg S month^{-1} in June 2018, but show less variability in the winter months, i.e. between 0.8 and 1.2 Gg S month^{-1} in December. Due to their comparably low surface area and the relatively low concentrations, high latitude regions do not play a significant role in globally integrated CS_2 emissions (Fig. 4). The dominance of southern temperate emissions of

260   CS_2, despite higher absolute mean concentrations in northern temperate regions is explained by the larger surface ocean area in the southern temperate regions (Fig. 4c and d).

4.3 Main drivers of interannual variability

The interannual variability in OCS and CS_2 concentrations and emissions is a result of the interannual variability in their

265   production and consumption processes, which in turn depends on environmental conditions. Globally integrated annual emissions of OCS correlate significantly with global annual averages of CDOM a_{350}, sea surface temperature and wind speed (Tab. 3). CDOM a_{350} explains the largest variance, and sea surface temperature and wind speed explain less of the observed variance. Thus, CDOM a_{350} has the strongest influence on the variability of global scale OCS concentrations. The influence is not surprising, as CDOM a_{350} impacts both photochemical and dark production of OCS and modulates the light field in the

270   water (at higher a_{350}, photoproduction is higher but also more limited to the surface). The photochemical production rate is second order dependent on CDOM a_{350}, reflecting its double role as photosensitizer, i.e. those molecules absorbing light energy for photochemical reactions, and as a proxy for the amount of sulfur molecules able to form radicals in photochemical reactions. As such, CDOM a_{350} exerts a strong, non-linear and positive influence on OCS concentration, and seems to be the main driver of its interannual variability. The overall strong influence of CDOM a_{350} on OCS interannual variability is also underlined by

275   similarity in the spatial pattern of the standard deviation in annual average concentrations and emissions between OCS and CDOM a_{350} (Fig. 5). Sea surface temperature strongly influences OCS hydrolysis, which leads to low concentrations in warm tropical and subtropical waters. Temperature also controls the solubility of the gas in water, i.e. the equilibrium water concentration is higher in colder waters. Variations in temperature explain a small part of interannual variations in OCS emissions. However, rising temperature towards the end of the period (Fig. 5) did not outweigh the increase in CDOM a_{350},

280   which supports the above mentioned result that the observed changes in CDOM a_{350} had a stronger influence on overall OCS production than observed temperature changes had on hydrolysis. Finally, wind speed imposes a nonlinear control on OCS emissions, but the impact is smaller than that of CDOM a_{350}.

Globally integrated CS_2 emissions correlate significantly with CDOM a_{350}, with a substantial part of the variance in interannual

285   variability (67%) explained by this single factor, although this is less than for OCS. Photochemical production of CS_2 is similarly calculated as that for OCS, and hence depends nonlinearly and positively on CDOM a_{350}. The lesser amount of explained variance compared to OCS may result from the lack of a CDOM a_{350} dependent dark production process.

Interestingly, CS$_2$ emissions correlate with temperature, although temperature is not part of any production or consumption process in the model, and solely modulates the solubility of CS$_2$. Increasing temperature decreases the solubility and would

290   lead to a lower surface water concentration, hence, this effect cannot explain the correlation between temperature and CS$_2$ surface concentrations in observations (Lennartz et al., 2020). Potentially, the co-variation of temperature with radiation dose might be responsible for the correlation of CS$_2$ concentration and temperature that is evident across observational datasets (see Introduction). The spatial variation of the standard deviation of annual averages of CS$_2$ concentration and emissions resembles that of CDOM a_{350}, again underlining that this is a major factor for interannual variability of CS$_2$ (Fig. 5).

295

4.4 Comparison to observations

The model output of the monthly resolved simulation for 2000-2019 is compared to the database compiled by Lennartz et al., (2020), which contains 2970 fully georeferenced OCS measurements and 501 fully georeferenced CS$_2$ measurements in the period considered here. The model output is subsampled at time (including time of day) and location closest to the

300   measurements in the respective period for a 1:1 comparison.

For OCS, the range of the subsampled model output agrees well with data from the database (7 cruises, n=2971), with a slight underestimation of measured concentrations by the model (average 40.1 pmol L^{-1} in the database, 38.4 pmol L^{-1} in the model, Fig. 6a). The direct comparison reveals remaining scatter around the 1:1 line, and a high bias in the model which grows with increasing OCS concentrations (Fig. 5b). The scatter and high bias in the data likely results from simplifications in the model.

305   The main simplifications, probably causing these discrepancies between observation and models, are the missing horizontal transport, the use of averaged wind speed as forcing, the use of CDOM a_{350} as a proxy for photochemical production and the application of a climatological mean for the depth of the mixed layer.

Using CDOM a_{350} as a proxy for OCS photochemical production may introduce some scatter, but likely not a systematic bias. The very complex nature of the dissolved organic matter pool in the ocean, which comprises CDOM as the optically active

310   fraction, makes it difficult to assign one photoproduction rate constant or apparent quantum yield to all the reactions taking place with different precursors. CDOM a_{350} has been shown to be a suitable proxy across three major ocean basins (Atlantic, Pacific, Indian Ocean), but the rate constant - CDOM a_{350} relationship showed some variability that might be improved when more data becomes available.

The missing horizontal transport can lead to a systematic model bias especially in cold waters where OCS lifetime increases

315   to time scales (days) relevant for physical transport, but still this process is unlikely to decouple OCS concentrations from its drivers like CDOM and temperature, that would be transported accordingly. The effect of horizontal transport is negligible in warm waters of the tropics, subtropics and most of the temperate regions. In regions with deep mixed layers such as the Southern Ocean, the assumption of a completely well mixed surface layer may be violated and cause discrepancies between the modelled value (average of mixed layer) and the measured value (close to surface, i.e. higher concentration that at bottom

320   of the mixed layer). Since the modelled concentration depends on depth of the mixed layer and its relation to the photic zone,

a climatological average as used here will introduce biases, however, detailed information on mixed layer depth in monthly resolution is not available. This simplification mainly affects OCS concentrations in high latitudes, where concentrations are relatively high, and thus might be partly responsible for the systematic bias revealed by the scatter plot in Fig. 5b. Furthermore, averaging wind speed to a mean monthly cycle will most likely lead to an underestimation of emissions and, hence, an

325 overestimation of concentrations. Due to the nonlinear relationship of the transfer velocity of the gas exchange with wind speed, averaging disproportionally reduces the effect of increased emissions during high wind speeds. Still, given these simplifications and assumptions, the overall good agreement with the measurements underlines the applicability of the model for assessing the marine cycling of OCS and its emissions to the atmosphere.

330 The marine cycling of CS_2 is less well understood than that of OCS. This relatively poorer process understanding is reflected by the comparison of the modelled CS_2 concentrations with those of the database (3 cruises, 501 measurements) (R^2=0.04). Modelled concentrations agree with observations on average (average database: 18.0 pmol L^{-1}, average subsampled model output: 18.2 pmol L^{-1}). While the cruises Poseidon 269 and ASTRA-OMZ are relatively well represented by the model (colour code in Fig. 6d), the variability of the measurements during Transpegaso is not well captured. The model used here has some

335 underlying assumptions and simplifications that call for refinement in the future when detailed process understanding is available. For example, the model is based on the assumption of a constant ratio between the apparent quantum yields of OCS and CS_2. It has been shown that this ratio is not always constant ((Kettle, 2000; Lennartz et al., 2019), but as the production pathways of both gases show some similarities (Modiri Gharehveran and Shah, 2018), the model formulation with a constant ratio is a first approximation. Second, the presence of a chemical sink is rationalised by its necessity to explain observed

340 concentrations along an Atlantic transect (Kettle, 2000; Lennartz et al., 2019), but has no mechanistic foundation so far. Dedicated laboratory experiments disentangling the source and sink processes in the water column are needed to further resolve this issue and to improve modelling efforts. Finally, this model does not consider any biological production of CS_2. This assumption is justified for a first approximation, as CDOM and primary production (photosynthesis) show similar global scale patterns. High CDOM will thus lead to high production of CS_2 in the water, even though the scaling of the photoproduction

345 rate constant (AQY) might inherently include biological production due to the covariation of photosynthesis patterns with CDOM and radiation. Overall, the presented CS_2 concentration and emissions are a first approximation, and more detailed process understanding is important to improve emission estimates.

The emission estimate of both gases includes further uncertainties introduced by the parameterizations of the transfer velocity used for calculation of air-sea exchange, which carry large uncertainties especially at high wind speeds (Wanninkhof, 2014).

350 Furthermore, emissions here are calculated based on the concentration gradient between surface water and the equilibrium concentration dictated by the atmospheric mixing ratio, without taking into account any potential effect of the sea surface microlayer. Whether and how the enrichment of surfactants in the sea surface microlayer affects emissions of these gases has not been sufficiently assessed to date.

5 Data and code availability

355 The code is available on github under https://github.com/Sinikka-L/OCS_CS2_boxmodel. The simulation output is available at zenodo 10.5281/zenodo.4297010 (Link: https://doi.org/10.5281/zenodo.4297010)(Lennartz et al., 2020a). The output consists of one netCDF files for each gas, each of a size of ca. 444 MB with monthly averages of sea surface concentrations and emissions to the atmosphere, as well as a mean diel cycle for each month.

6 Summary and Conclusions

360 OCS and CS_2 are climate relevant trace gases and OCS can also be used as a proxy to infer terrestrial gross primary production. A missing source in the atmospheric OCS budget currently makes conclusions on the future impact on both gases and the application of this proxy on a global scale difficult. Since both gases contribute to the atmospheric OCS budget, their oceanic emissions have been suggested previously to account for that missing source. We provide monthly resolved OCS and CS_2 concentration and marine emission data for the period 2000-2019 based on a mechanistic ocean box model. We show that

365 interannual variability of OCS is smaller than its seasonal variability in globally integrated emissions, but that a significant positive trend is evident across the period 2000-2019. The main driver for interannual variabilities is variation in CDOM a_{350}. The comparison of our data to a database with more than 2500 measurements reveals an overall good agreement. The CS_2 model presented here for the first time is a first approximation and reveals stronger interannual variability than seasonal variability of emissions. Again, CDOM (or indirectly, biological production) seems to be strongly influencing concentration

370 and emission patterns of CS_2. Similarly, an increasing trend in CS_2 emissions is significant for the period 2000-2019. We encourage the use of the data provided here as input for atmospheric modelling studies to further assess the atmospheric OCS budget and the role of OCS in climate.

Acknowledgements

375 The authors thank the Ocean Biology and Processing Group at NASA Goddard Space Flight Center for access to the Aqua MODIS data as well as ECMWF for access to the ERA5 data.

References

380   Berry, J., Wolf, A., Campbell, J. E., Baker, I., Blake, N., Blake, D., Denning, A. S., Kawa, S. R., Montzka, S. A., Seibt, U., Stimler, K., Yakir, D. and Zhu, Z.: A coupled model of the global cycles of carbonyl sulfide and CO_2: A possible new window on the carbon cycle, J. Geophys. Res. Biogeosciences, 118(2), 842–852, doi:10.1002/jgrg.20068, 2013.

Brühl, C., Lelieveld, J., Crutzen, P. J. and Tost, H.: The role of carbonyl sulphide as a source of stratospheric sulphate aerosol and its impact on climate, Atmos. Chem. Phys., 12(3), 1239–1253, doi:10.5194/acp-12-1239-2012, 2012.

385   De Bruyn, W. J., Swartz, E., Hu, J. H., Shorter, J. A., Davidovits, P., Worsnop, D. R., Zahniser, M. S. and Kolb, C. E.: Henry's law solubilities and Śetchenow coefficients for biogenic reduced sulfur species obtained from gas-liquid uptake measurements, J. Geophys. Res., 100(D4), 7245–7251, doi:10.1029/95JD00217, 1995.

Chin, M. and Davis, D. D.: Global sources and sinks of OCS and CS_2 and their distributions, Global Biogeochem. Cycles, 7(2), 321–337, doi:10.1029/93GB00568, 1993.

390   Cutter, G. A. and Radford-Knoery, J.: Carbonyl sulfide in two estuaries and shelf waters of the western North Atlantic Ocean, Mar. Chem., 43(1–4), 225–233, doi:10.1016/0304-4203(93)90228-G, 1993.

Cutter, G. A., Cutter, L. S. and Filippino, K. C.: Sources and cycling of carbonyl sulfide in the Sargasso Sea, Limnol. Oceanogr., 49(2), 555–565, doi:10.4319/lo.2004.49.2.0555, 2004.

EEA 1/2017: Climate Change, impacts and vulnerability in Europe 2016 - an indicator based report, Copenhagen, Denmark.,
395   2017.

Elliott, S.: Effect of hydrogen peroxide on the alkaline hydrolysis of carbon disulfide, Environ. Sci. Technol., 24(2), 264–267, doi:10.1021/es00072a017, 1990.

Elliott, S., Lu, E. and Rowland, F. S.: Carbonyl sulfide hydrolysis as a source of hydrogen sulfide in open ocean seawater, Geophys. Res. Lett., 14(2), 131–134, doi:10.1029/GL014i002p00131, 1987.

400   Elliott, S., Lu, E. and Rowland, F. S.: Rates and mechanisms for the hydrolysis of carbonyl sulfide in natural waters, Environ. Sci. Technol., 23(4), 458–461, doi:10.1021/es00181a011, 1989.

Ferek, R. J. and Andreae, M. O.: The supersaturation of carbonyl sulfide in surface waters of the Pacific Ocean off Peru, Geophys. Res. Lett., 10(5), 393–396, doi:10.1029/GL010i005p00393, 1983.

Ferek, R. J. and Andreae, M. O.: Photochemical production of carbonyl sulphide in marine surface waters, Nature, 307(5947),
405   148–150, doi:10.1038/307148a0, 1984.

Glatthor, N., Höpfner, M., Baker, I. T., Berry, J., Campbell, J. E., Kawa, S. R., Krysztofiak, G., Leyser, A., Sinnhuber, B.-M., Stiller, G. P., Stinecipher, J. and von Clarmann, T.: Tropical sources and sinks of carbonyl sulfide observed from space, Geophys. Res. Lett., 42(22), 10,082-10,090, doi:10.1002/2015GL066293, 2015.

Hayduk, W. and Laudie, H.: Prediction of diffusion coefficients for nonelectrolytes in dilute aqueous solutions, AIChE J.,
410   20(3), 611–615, doi:10.1002/aic.690200329, 1974.

von Hobe, M., Cutter, G. A., Kettle, A. J. and Andreae, M. O.: Dark production: A significant source of oceanic COS, J.

Geophys. Res. Ocean., 106(C12), 31217–31226, doi:10.1029/2000JC000567, 2001.

von Hobe, M., Najjar, R. G., Kettle, A. J. and Andreae, M. O.: Photochemical and physical modeling of carbonyl sulfide in the ocean, J. Geophys. Res., 108(C7), 3229, doi:10.1029/2000JC000712, 2003.

415 Kamyshny, A. J., Goifman, A., Rizkov, D. and Lev, O.: Formation of Carbonyl Sulfide by the Reaction of Carbon Monoxide and Inorganic Polysulfides, , doi:10.1021/ES0201911, 2003.

Kettle, A. J.: Extrapolations of the Flux of Dimethylsulfide, Carbon Monoxide, Carbonyl Sulfide and Carbon Disulfide from the Oceans, York University., 2000.

Kettle, A. J., Rhee, T. S., von Hobe, M., Poulton, A., Aiken, J. and Andreae, M. O.: Assessing the flux of different volatile

420 sulfur gases from the ocean to the atmosphere, J. Geophys. Res. Atmos., 106(D11), 12193–12209, doi:10.1029/2000JD900630, 2001.

Kettle, A. J., Kuhn, U., von Hobe, M. von, Kesselmeier, J. and Andreae, M. O.: Global budget of atmospheric carbonyl sulfide: Temporal and spatial variations of the dominant sources and sinks, J. Geophys. Res., 107(D22), 4658, doi:10.1029/2002JD002187, 2002.

425 Khalil, M. A. K. and Rasmussen, R. A.: Global sources, lifetimes and mass balances of carbonyl sulfide (OCS) and carbon disulfide (CS2) in the earth's atmosphere, Atmos. Environ., 18(9), 1805–1813, doi:10.1016/0004-6981(84)90356-1, 1984.

Kremser, S., Thomason, L. W., von Hobe, M., Hermann, M., Deshler, T., Timmreck, C., Toohey, M., Stenke, A., Schwarz, J. P., Weigel, R., Fueglistaler, S., Prata, F. J., Vernier, J.-P., Schlager, H., Barnes, J. E., Antuña-Marrero, J.-C., Fairlie, D., Palm, M., Mahieu, E., Notholt, J., Rex, M., Bingen, C., Vanhellemont, F., Bourassa, A., Plane, J. M. C., Klocke, D., Carn, S. A.,

430 Clarisse, L., Trickl, T., Neely, R., James, A. D., Rieger, L., Wilson, J. C. and Meland, B.: Stratospheric aerosol-Observations, processes, and impact on climate, Rev. Geophys., 54(2), 278–335, doi:10.1002/2015RG000511, 2016.

Ksionzek, K. B., Lechtenfeld, O. J., McCallister, S. L., Schmitt-Kopplin, P., Geuer, J. K., Geibert, W. and Koch, B. P.: Dissolved organic sulfur in the ocean: Biogeochemistry of a petagram inventory., Science, 354(6311), 456–459, doi:10.1126/science.aaf7796, 2016.

435 Kuai, L., Worden, J. R., Campbell, J. E., Kulawik, S. S., Li, K.-F., Lee, M., Weidner, R. J., Montzka, S. A., Moore, F. L., Berry, J. A., Baker, I., Denning, A. S., Bian, H., Bowman, K. W., Liu, J. and Yung, Y. L.: Estimate of carbonyl sulfide tropical oceanic surface fluxes using Aura Tropospheric Emission Spectrometer observations, J. Geophys. Res. Atmos., 120(20), 11,012-11,023, doi:10.1002/2015JD023493, 2015.

Lana, A., Bell, T. G., Simó, R., Vallina, S. M., Ballabrera-Poy, J., Kettle, A. J., Dachs, J., Bopp, L., Saltzman, E. S., Stefels,

440 J., Johnson, J. E. and Liss, P. S.: An updated climatology of surface dimethlysulfide concentrations and emission fluxes in the global ocean, Global Biogeochem. Cycles, 25(1), n/a-n/a, doi:10.1029/2010GB003850, 2011.

Lennartz, S., Gauss, M., von Hobe, M. and Marandino, C.: Carbonyl Sulfide (OCS/COS) and Carbon Disulfide (CS2): global modelled marine surface concentrations and emissions, 2000-2019, , doi:10.5281/ZENODO.4297010, 2020a.

Lennartz, S. T., Marandino, C. A., von Hobe, M., Cortes, P., Quack, B., Simo, R., Booge, D., Pozzer, A., Steinhoff, T., Arevalo-

445 Martinez, D. L., Kloss, C., Bracher, A., Röttgers, R., Atlas, E. and Krüger, K.: Direct oceanic emissions unlikely to account

for the missing source of atmospheric carbonyl sulfide, Atmos. Chem. Phys., 17(1), 385–402, doi:10.5194/acp-17-385-2017, 2017.

Lennartz, S. T., von Hobe, M., Booge, D., Bittig, H. C., Fischer, T., Gonçalves-Araujo, R., Ksionzek, K. B., Koch, B. P., Bracher, A., Röttgers, R., Quack, B. and Marandino, C. A.: The influence of dissolved organic matter on the marine production
450 of carbonyl sulfide (OCS) and carbon disulfide (CS<sub>2</sub>) in the Peruvian upwelling, Ocean Sci., 15(4), 1071–1090, doi:10.5194/os-15-1071-2019, 2019.

Lennartz, S. T., Marandino, C. A., von Hobe, M., Andreae, M. O., Aranami, K., Atlas, E., Berkelhammer, M., Bingemer, H., Booge, D., Cutter, G., Cortes, P., Kremser, S., Law, C. S., Marriner, A., Simó, R., Quack, B., Uher, G., Xie, H. and Xu, X.: Marine carbonyl sulfide (OCS) and carbon disulfide (CS2): a compilation of measurements in seawater and the marine
455 boundary layer, Earth Syst. Sci. Data, 12(1), 591–609, doi:10.5194/essd-12-591-2020, 2020b.

Levitus, S., Boyer, T. P., Garcia, H. E., Locarnini, R. A., Zweng, M. M., Mishonov, A. V., Reagan, J. R., Antonov, J. I., Baranova, O. K., Biddle, M., Hamilton, M., Johnson, D. R., Paver, C. R. and Seidov, D.: World Ocean Atlas 2013 (NCEI Accession 0114815). [Salinity]., NOAA Natl. Centers Environ. Information. Dataset., doi:https://doi.org/10.7289/v5f769gt, 2013.

460 Modiri Gharehveran, M. and Shah, A. D.: Indirect Photochemical Formation of Carbonyl Sulfide and Carbon Disulfide in Natural Waters: Role of Organic Sulfur Precursors, Water Quality Constituents, and Temperature, Environ. Sci. Technol., 52(16), 9108–9117, doi:10.1021/acs.est.8b01618, 2018.

Montzka, S. A., Calvert, P., Hall, B. D., Elkins, J. W., Conway, T. J., Tans, P. P. and Sweeney, C.: On the global distribution, seasonality, and budget of atmospheric carbonyl sulfide (COS) and some similarities to CO $_2$, J. Geophys. Res., 112(D9),
465 D09302, doi:10.1029/2006JD007665, 2007.

NASA Goddard Space Flight Center: Moderate-resolution Imaging Spectroradiometer (MODIS) Aqua Inherent Optical Properties Data; 2018 Reprocessing. NASA OB.DAAC, Greenbelt, MD, USA. Accessed on 06/12/2020, doi data/10.5067/AQUA/MODIS/L3M/IOP/2003 to, 2019.

NCAR: The Climate Data Guide: Common Spectral Model Grid Resolutions, Natl. Cent. Atmos. Res. Staff [online] Available
470 from: https://climatedataguide.ucar.edu/climate-model-evaluation/common-spectral-model-grid-resolutions (Accessed 3 December 2020), 2017.

Nightingale, P. D., Malin, G., Law, C. S., Watson, A. J., Liss, P. S., Liddicoat, M. I., Boutin, J. and Upstill-Goddard, R. C.: In situ evaluation of air-sea gas exchange parameterizations using novel conservative and volatile tracers, Global Biogeochem. Cycles, 14(1), 373–387, doi:10.1029/1999GB900091, 2000.

475 Pos, W. H., Riemer, D. D. and Zika, R. G.: Carbonyl sulfide (OCS) and carbon monoxide (CO) in natural waters: evidence of a coupled production pathway, Mar. Chem., 62(1–2), 89–101, doi:10.1016/S0304-4203(98)00025-5, 1998.

Rasmussen, R. A., Khalil, M. A. K. and Hoyt, S. D.: The oceanic source of carbonyl sulfide (OCS), Atmos. Environ., 16(6), 1591–1594, doi:10.1016/0004-6981(82)90111-1, 1982.

Schmidtko, S., Johnson, G. C. and Lyman, J. M.: MIMOC: A global monthly isopycnal upper-ocean climatology with mixed

480   layers, J. Geophys. Res. Ocean., 118(4), 1658–1672, doi:10.1002/jgrc.20122, 2013.

Solomon, S., Daniel, J. S., Neely, R. R., Vernier, J.-P., Dutton, E. G. and Thomason, L. W.: The Persistently Variable "Background" Stratospheric Aerosol Layer and Global Climate Change, Science (80-.)., 333(6044), 866 LP – 870, doi:10.1126/science.1206027, 2011.

Solomon, S., Kinnison, D., Bandoro, J. and Garcia, R.: Simulation of polar ozone depletion: An update, J. Geophys. Res.

485   Atmos., 120(15), 7958–7974, doi:10.1002/2015JD023365, 2015.

Stickel, R. E., Chin, M., Daykin, E. P., Hynes, A. J., Wine, P. H. and Wallington, T. J.: Mechanistic studies of the hydroxyl-initiated oxidation of carbon disulfide in the presence of oxygen, J. Phys. Chem., 97(51), 13653–13661, doi:10.1021/j100153a038, 1993.

Stimler, K., Montzka, S. A., Berry, J. A., Rudich, Y. and Yakir, D.: Relationships between carbonyl sulfide (COS) and CO_2

490   during leaf gas exchange, New Phytol., 186(4), 869–878, doi:10.1111/j.1469-8137.2010.03218.x, 2010.

Suntharalingam, P., Kettle, A. J., Montzka, S. M. and Jacob, D. J.: Global 3-D model analysis of the seasonal cycle of atmospheric carbonyl sulfide: Implications for terrestrial vegetation uptake, Geophys. Res. Lett., 35(19), L19801, doi:10.1029/2008GL034332, 2008.

Turco, R. P., Whitten, R. C., Toon, O. B., Pollack, J. B. and Hamill, P.: OCS, stratospheric aerosols and climate, Nature,

495   283(5744), 283–285, doi:10.1038/283283a0, 1980.

Wanninkhof, R.: Relationship between wind speed and gas exchange over the ocean revisited, Limnol. Oceanogr. Methods, 12(6), 351–362, doi:10.4319/lom.2014.12.351, 2014.

Watts, S. F.: The mass budgets of carbonyl sulfide, dimethyl sulfide, carbon disulfide and hydrogen sulfide, Atmos. Environ., 34(5), 761–779, doi:10.1016/S1352-2310(99)00342-8, 2000.

500   Weiss, P. S., Andrews, S. S., Johnson, J. E. and Zafiriou, O. C.: Photoproduction of carbonyl sulfide in South Pacific Ocean waters as a function of irradiation wavelength, Geophys. Res. Lett., 22(3), 215–218, doi:10.1029/94GL03000, 1995a.

Weiss, P. S., Johnson, J. E., Gammon, R. H. and Bates, T. S.: Reevaluation of the open ocean source of carbonyl sulfide to the atmosphere, J. Geophys. Res., 100(D11), 23083–23092, doi:10.1029/95jd01926, 1995b.

Whelan, M. E., Lennartz, S. T., Gimeno, T. E., Wehr, R., Wohlfahrt, G., Wang, Y., Kooijmans, L. M. J., Hilton, T. W., Belviso,

505   S., Peylin, P., Commane, R., Sun, W., Chen, H., Kuai, L., Mammarella, I., Maseyk, K., Berkelhammer, M., Li, K.-F., Yakir, D., Zumkehr, A., Katayama, Y., Ogée, J., Spielmann, F. M., Kitz, F., Rastogi, B., Kesselmeier, J., Marshall, J., Erkkilä, K.-M., Wingate, L., Meredith, L. K., He, W., Bunk, R., Launois, T., Vesala, T., Schmidt, J. A., Fichot, C. G., Seibt, U., Saleska, S., Saltzman, E. S., Montzka, S. A., Berry, J. A. and Campbell, J. E.: Reviews and syntheses: Carbonyl sulfide as a multi-scale tracer for carbon and water cycles, Biogeosciences, 15(12), 3625–3657, doi:10.5194/bg-15-3625-2018, 2018.

510   Xie, H. and Moore, R. M.: Carbon disulfide in the North Atlantic and Pacific oceans, J. Geophys. Res. Ocean., 104(C3), 5393–5402, doi:10.1029/1998JC900074, 1999.

Xie, H., Moore, R. M. and Miller, W. L.: Photochemical production of carbon disulphide in seawater, J. Geophys. Res. Ocean., 103(C3), 5635–5644, doi:10.1029/97jc02885, 1998.

Xie, H., Scarratt, M. G. and Moore, R. M.: Carbon disulphide production in laboratory cultures of marine phytoplankton,

515 Atmos. Environ., 33(21), 3445–3453, doi:10.1016/S1352-2310(98)00430-0, 1999.

Zepp, R. G. and Andreae, M. O.: Factors affecting the photochemical production of carbonyl sulfide in seawater, Geophys. Res. Lett., 21(25), 2813–2816, doi:10.1029/94GL03083, 1994.

Figures

a)   b)
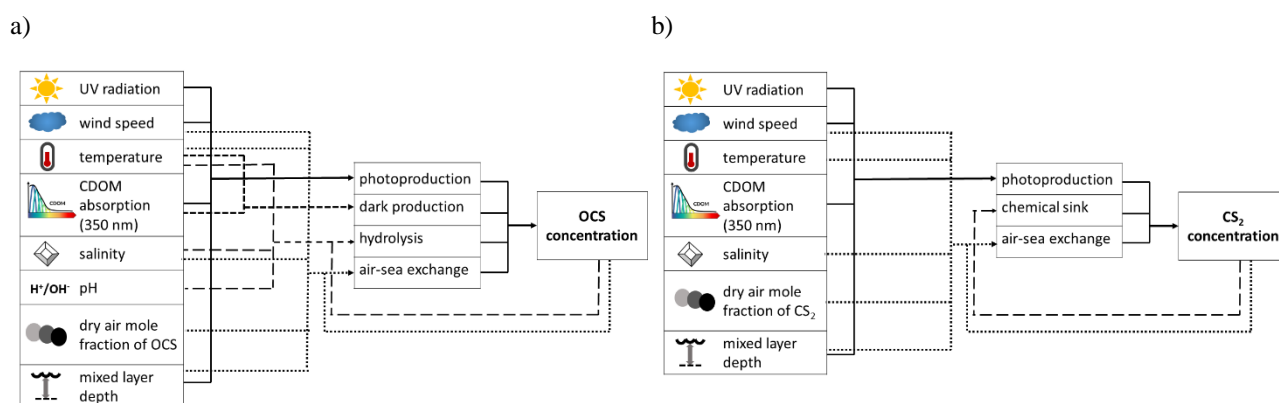
Figure 1: Schematic overview on processes and forcing included in the box models for a) OCS and b) CS$_2$.

520

a)
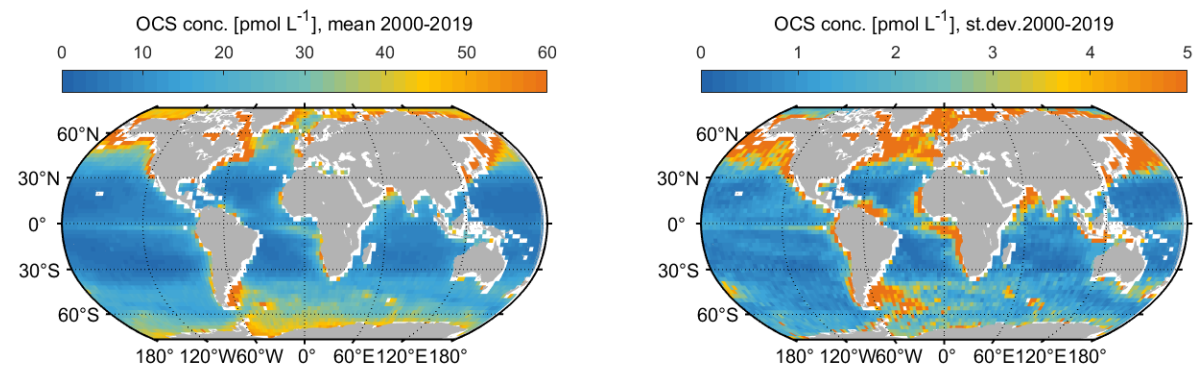
b)
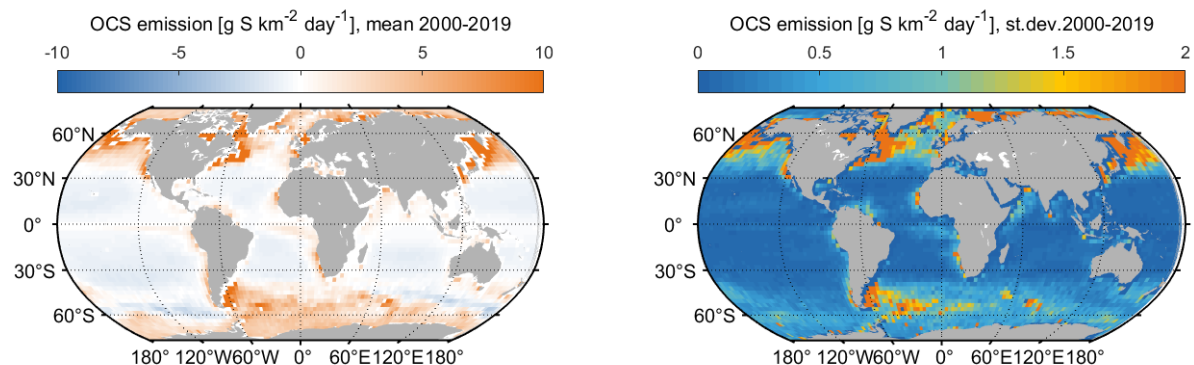
c)
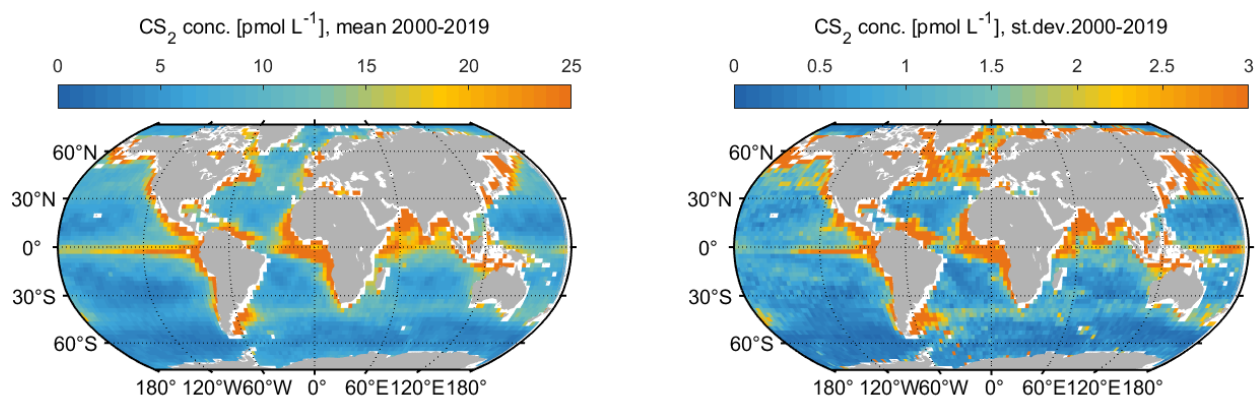
d)
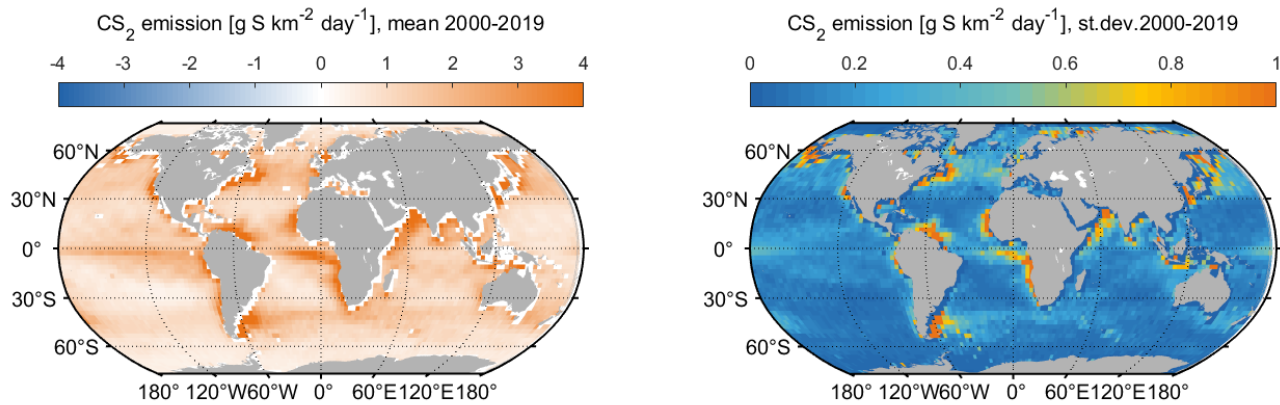
Figure 2: Spatial variation of a) mean OCS surface concentration (left panel) and standard deviation of annual mean concentrations (right panel), b) same for OCS emissions, c) same for CS$_2$ surface concentration, d) same for CS$_2$ emissions, averaged over the 2000-2019 period.

525
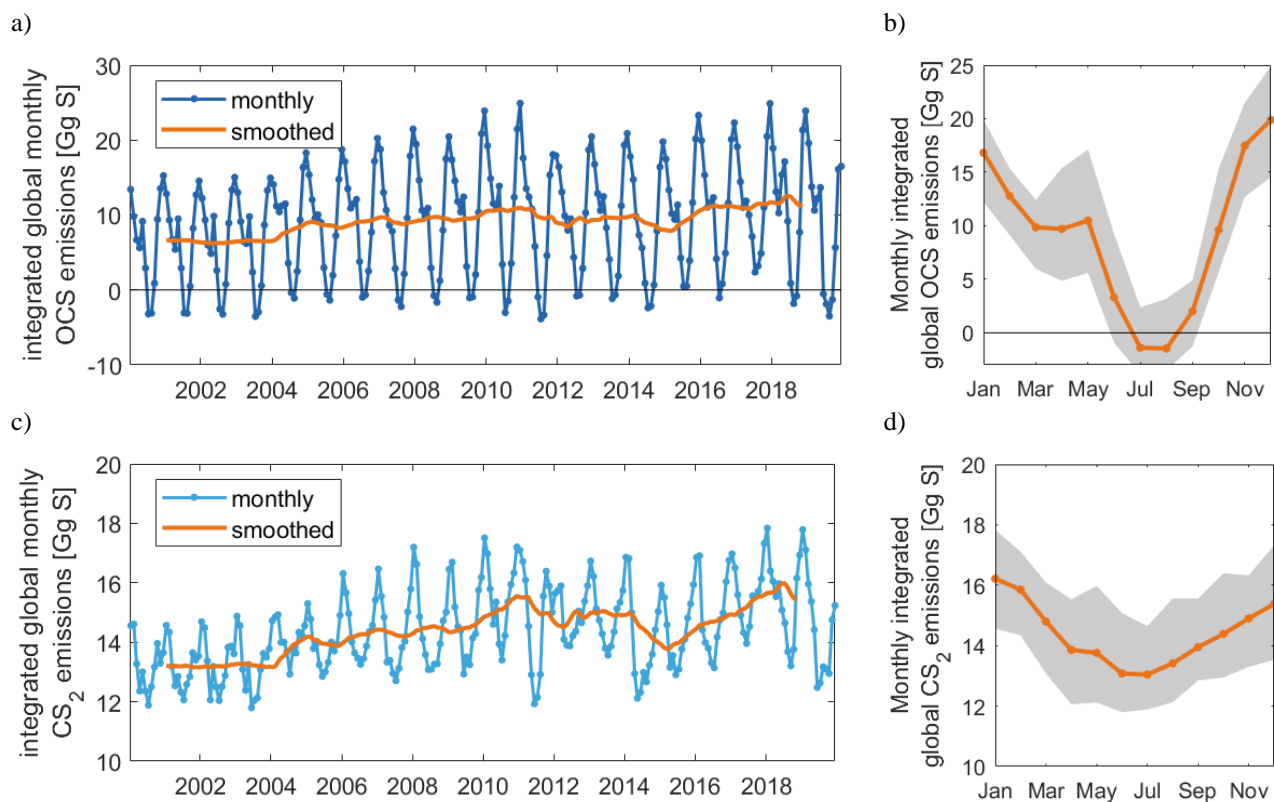
Figure 3: Interannual variability of OCS emissions as time series (a) and mean annual cycle in orange, standard deviation of respective month in shaded grey area (b); (c) and (d) same as (a) and (b) but for CS$_2$. The model output is saved in 2-hour intervals for the 15th of each month, and integrated over 30 days for the monthly emissions shown here.

530

a)
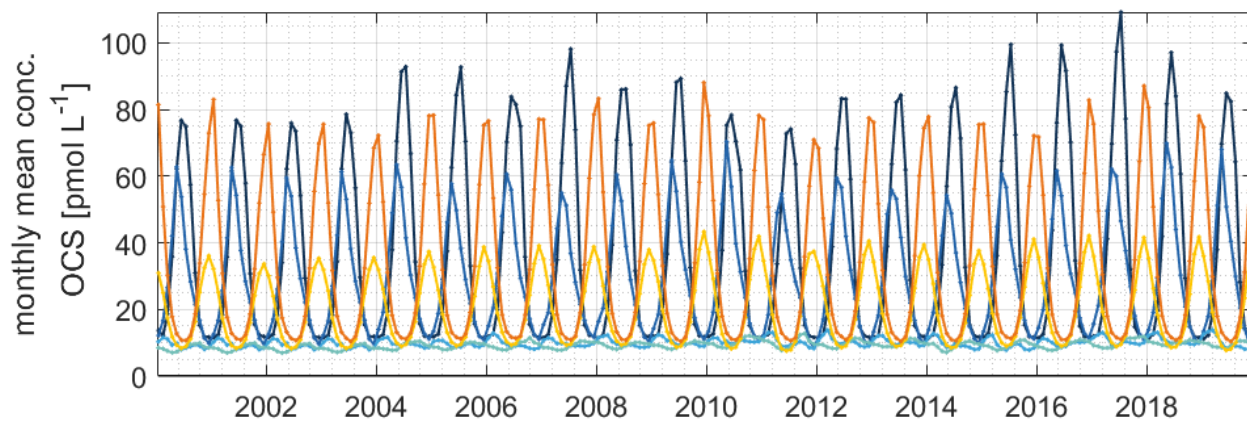
b)
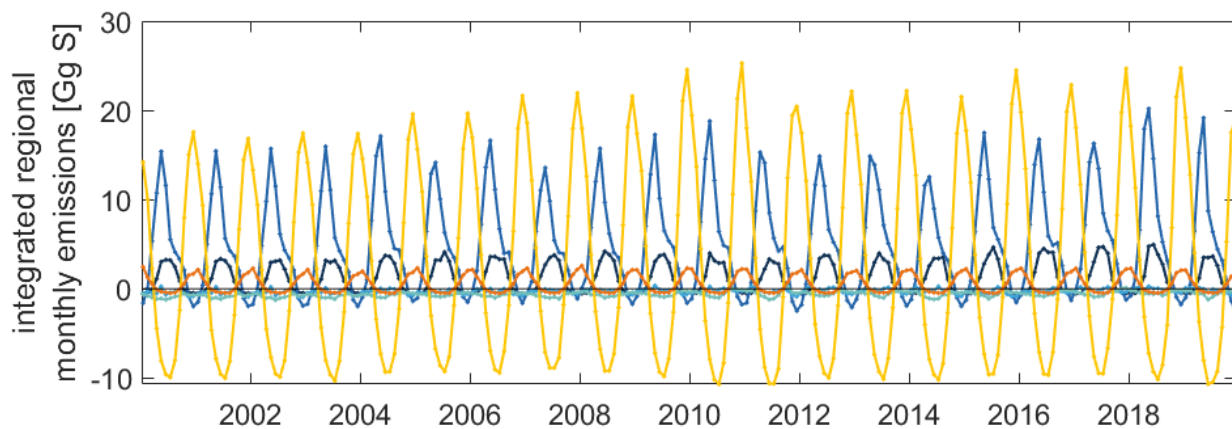
c)
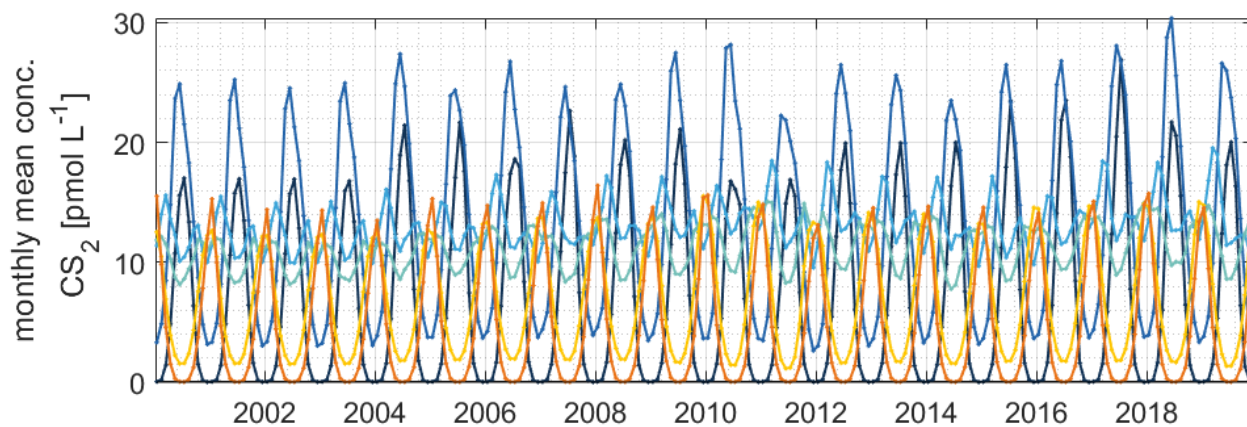
d)
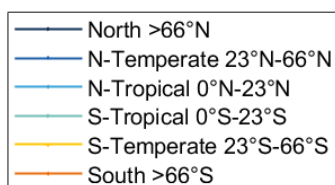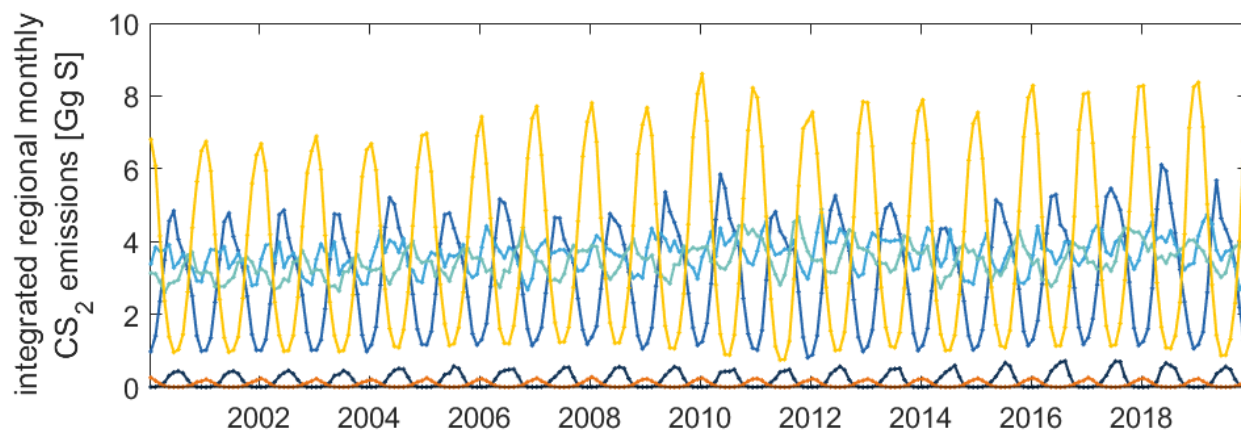
Figure 4: Regionally resolved interannual variability of concentrations (a) and emissions (b) for OCS. Same in (c) and (d) for CS₂.

535

a)

b)

c)
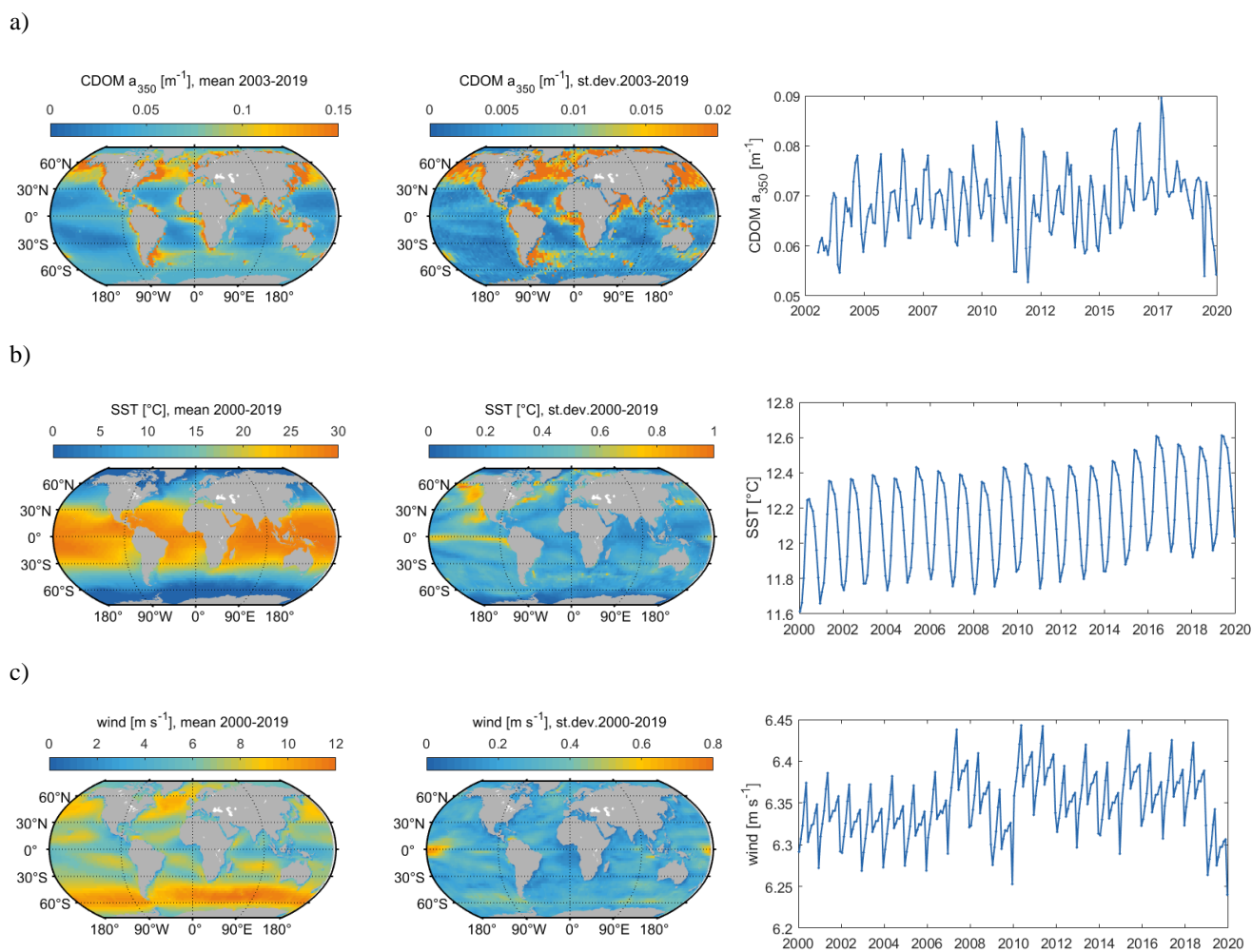
Figure 5: Mean and standard deviation (maps) and interannual variation (right panels) of model input parameters: (a) CDOM a350, (b) sea surface temperature, (c) wind speed. Data sources listed in Tab. 1.

540
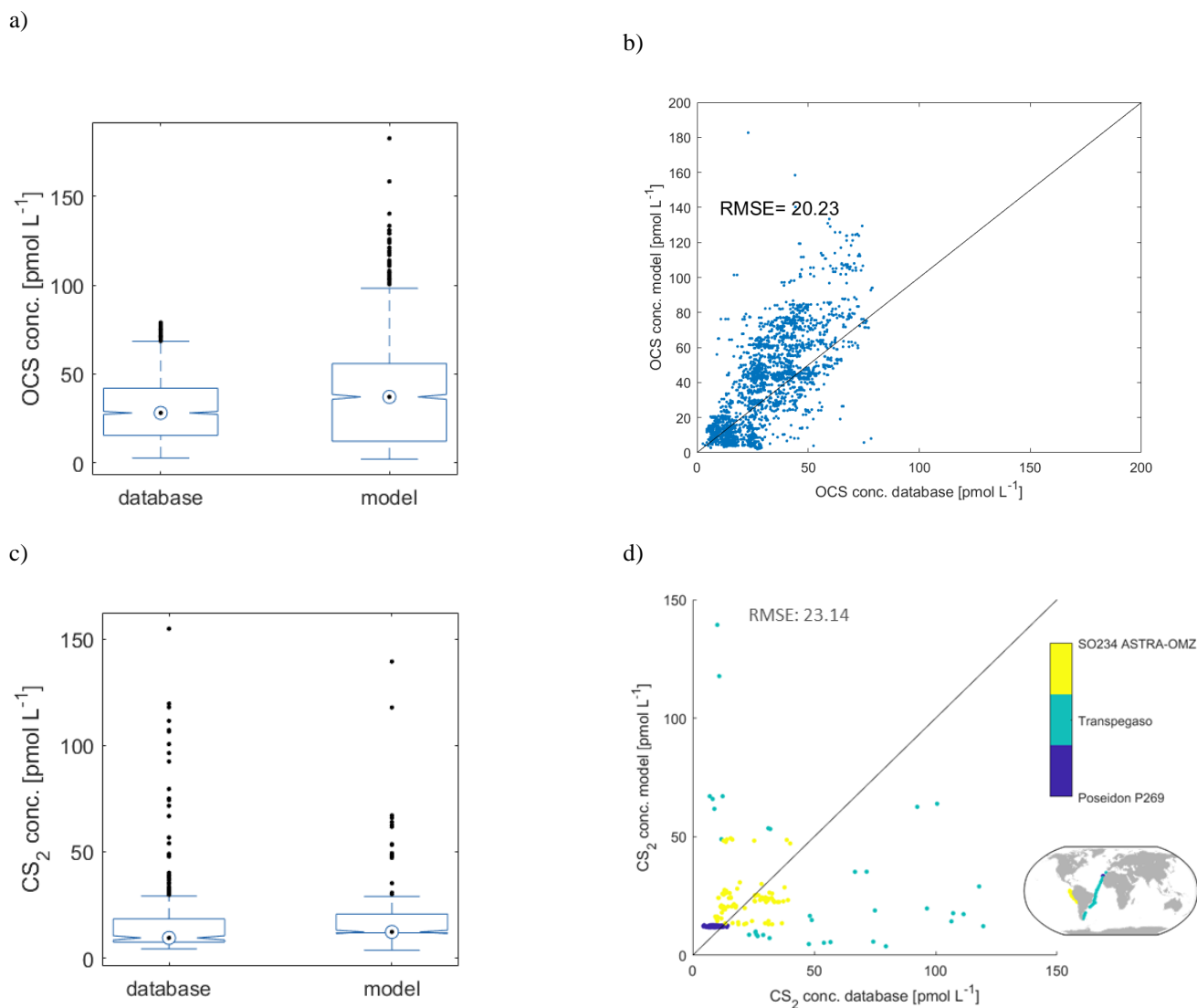
Figure 6: Comparison of model-output to observations from the database described in Lennartz et al., (2020). a) Box plot of OCS reference data from database and subsampled model output at time and location of measurements (32 cruises) b) scatter plot of 1:1 comparison with same data as in a), black line is 1:1 line, c) and d) same as a) and b) but for CS2 (3 cruises).

Tables

545 **Table 1: Overview on forcing parameters, their resolution and sources used for the box model simulations 2000-2019.**

Parameter	Resolution	Source
Absorption coefficient of CDOM at 350 nm (a350)	gridded, monthly resolution	Aqua MODIS satellite data, monthly composite of absorption due to gelbstof and detritus at 443, converted to 350 nm with a reference slope of 0.02. Note that years 2000-2002 are the same as 2003, as data is only available from late 2002 onwards. (NASA Goddard Space Flight Center, 2019)
Surface temperature	gridded, monthly resolution with mean diurnal cycle	ERA5 reanalysis (Hersbach et al., 2018), variable name in ERA5: 'skin temperature'
Salinity	gridded, climatological monthly mean	World Ocean Atlas 2013 (Levitus et al., 2013)
Global radiation (converted to UV radiation)	gridded, monthly resolution with mean diurnal cycle	ERA5 reanalysis (Hersbach et al., 2018), variable name in ERA5: 'surface solar radiation downwards'
Wind speed at surface	gridded, monthly resolution with mean diurnal cycle	ERA5 reanalysis (Hersbach et al., 2018), variable name in ERA5: 'u='10m u-component of wind' and v='10m v-component of wind' (for this study these were converted into total wind speed = sqrt(u^2+v^2))
pH	constant value (8.1)	
Mixed layer depth	gridded, climatological monthly mean	MIMOC climatology (Schmidtko et al., 2013)
Dry air mole fraction OCS	constant value, 500 ppt	
Dry air mole fraction CS$_2$	constant value, 0 ppt	
Sea surface pressure	gridded, monthly resolution with mean diurnal cycle	ERA5 reanalysis (Hersbach et al., 2018), variable name in ERA5: 'surface pressure'

550

Table 2: Globally integrated annual emissions of OCS and CS2 for each year in 2000-2019, together with descriptive statistics and trends.

	OCS	CS$_2$
	Gg S	Gg S
2000*	81.3	160.8
2001*	77.3	160.0
2002*	78.0	161.2
2003	78.8	160.3
2004	108.3	172.0
2005	100.8	169.1
2006	116.3	175.3
2007	110.6	173.4
2008	114.4	175.0
2009	126.3	179.7
2010	133.3	189.2
2011	109.0	179.5
2012	113.3	181.2
2013	117.9	181.3
2014	97.2	170.1
2015	127.6	175.0
2016	134.7	181.5
2017	142.1	189.7
2018	136.9	187.8
2019	102.0	177.3
mean	**110.3**	**174.97**
standard deviation	**20.3**	**9.3**
slope (only 2003-2019)	**1.7 Gg S yr^{-1}**	**0.95 Gg S yr^{-1}**
p slope (only 2003-2019)	**0.028**	**0.0067**

*CDOM from 2003

555

Table 3: Explained Variance (Pearson's R²) and significance level p for correlations of globally integrated emissions for OCS and CS₂ with global annual averages of CDOM a₃₅₀. sea surface temperature (SST) and wind speed. Significant results (α=0.01) are indicated in bold font.

560

	CS$_2$	CDOM a_{350}	SST	wind
OCS	**R^2=0. 87** **p=2.1e-9**	**R^2=0.94** **p=1.0e-10**	**R^2=0.41** **p=0.0024**	**R^2=0.32** **p=0.0099**
CS$_2$	1	**R^2=0.67** **p=6.0e-5**	**R^2=0.40** **p=0.0026**	R^2=0.29 p=0.0136
CDOM a350		1	R^2=0.23 p=0.051	R^2=0.22 p=0.0572
SST			1	R^2=0.02 p=0.53